High-accuracy radiation pressure models for the Lunar Reconnaissance Orbiter

Dominik Stiller

B.Sc. Student, Faculty of Aerospace Engineering, TU Delft, Netherlands

Abstract

Centimeter-scale orbit determination is necessary for satellite navigation and spaceborne geodesy. Orbits are sensitive to perturbations such as radiation pressure (RP) due to solar radiation as well as planetary albedo and thermal emissions. This project investigated sensitivities of orbit predictions to varying complexity in RP models for the Lunar Reconnaissance Orbiter (LRO). We found that solar RP dominates but lunar RP affects secular variations in semi-major axis and argument of periapsis. A constant-albedo lunar model and a paneled LRO model are recommended for precise radial and along-track positioning.

Keywords

Radiation pressure, orbit determination

Acronyms: BRDF bidirectional reflectance distribution function; LRO Lunar Reconnaissance Orbiter; RP radiation pressure

1 Introduction

Describe LRO mission Describe need for POD

sub-meter accuracy in radial component [1] 50-100 m in total position [2]

figure with magnitudes of perturbations

"SRP is the largest non-gravitational perturbation affecting the LRO orbit and inadequate modeling of SRP is the primary cause of large prediction errors for LRO, particularly during high-beta angle periods" [3] albedo modeling on moon necessary for selenodetic mapping [4] albedo radiation significant on moon since no atmosphere exists and surface of lunar highlands is rather reflective % [4] High OD error during full-sun periods with cannonball model, but acceptable with multi-panel model and real attitude for SA and HGA [5]

present similar papers like VielbergKusche

in this paper, only investigate orbital variations over 2.5 day arc -¿ goal is to improve force models for POD Long-term effect of RP would also be interesting (forces could cancel out over time or always act in same direction), but not considered here

Tudat is used and models are used for future research

2 General radiation pressure modeling

2.1 Mechanics of radiation pressure

RP results from the momentum transfer between electromagnetic radiation and a surface. A spacecraft may receive such radiation from the Sun but also from other celestial bodies: planets and moons emit albedo radiation through reflection of sunlight and thermal radiation depending on surface temperature. The RP exerts a force on the spacecraft governed by surface properties such as area, reflectivity and absorptivity. The resulting acceleration is the result of a complex interplay of the bodies emitting radiation (the "sources") and the spacecraft receiving the radiation (the "target").

Radiation can characterized by the radiant flux density, which commonly has units of $\mathrm{W/m^2}$. Radiosity is the *emitted and reflected* radiant flux density of an opaque surface. The irradiance E is the *incident* radiant flux density on a surface and provides a convenient way to decouple source and target models: the irradiance and the direction of incidence are sufficient to determine the target acceleration, independent of the actual source. We can combine this information into a vector quantity which we call directional irradiance $\mathbf{E} = E\hat{\mathbf{r}}_{t/s}$, where $\hat{\mathbf{r}}_{t/s}$ is the unit vector in the source–to–target direction. One or more directional irradiances, which can be though of as light rays, are the output of a source model and used as input to the target model. The RP exerted on an irradiated surface is proportional to $1/c$, where $c = 299\,792\,458\,\mathrm{m/s}$ is the speed of light. Given the magnitude of c, RP is usually small (around $4.5 \times 10^{-6}\,\mathrm{N/m^2}$ for solar radiation at Earth, where $E = 1361\,\mathrm{W/m^2}$ [6]).

Electromagnetic radiation is often composed not just of a single wavelength but rather a range of wavelengths. The distribution can be described by the spectral irradiance in units of $\mathrm{W/(m^2\,Hz)}$. Since surface properties are often wavelength-dependent, the target model would also have to be aware of the distribution. However, the surface properties as a function of wavelength are often not known, which is also the case for LRO. Therefore, we assume the irradiance from source models to be integrated over the whole spectrum and the surface properties of the target model to be valid for all wavelengths.

2.2 Reflectance distribution

Describing the reflectance of a surface is key to RP modeling. Both the way a source reflects sunlight and the direction a

[0]Email: dstiller@uw.edu

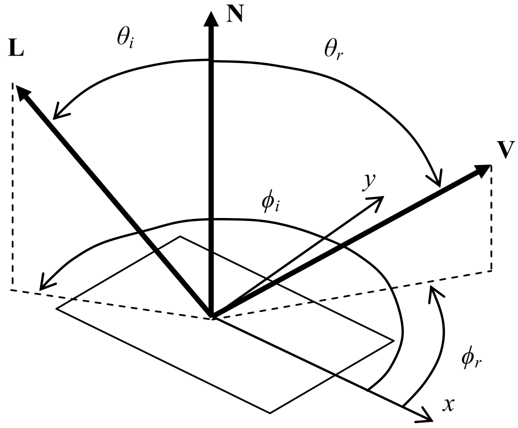

Figure 1. Geometry of a BRDF for a surface with normal $\mathbf{N}$, incoming direction $\mathbf{L}$, and observer direction $\mathbf{V}$. The viewing angle θ_r is between $\mathbf{V}$ and $\mathbf{N}$. Adapted from [7].

target is accelerated in depend on the angular distribution of reflectance.

General reflectance distribution In general, reflectance comprises a diffuse (scattered in many directions) and a specular (mirror-like) component. The remaining energy is absorbed by the surface. The reflectance varies with surface normal $\mathbf{N}$, incoming radiation direction $\mathbf{L}$, and observer direction $\mathbf{V}$. This geometry is shown in Figure 1. A bidirectional reflectance distribution function (BRDF) describes the fraction of irradiance reflected towards the observer per steradian, i.e. [7]

$$f_r(\theta_i, \phi_i, \theta_r, \phi_r) = \frac{dL_r(\theta_r, \phi_r)}{dE_j(\theta_i, \phi_i)}, \tag{1}$$

where dL_r is the reflected radiance (the directional counterpart to radiosity, typically in $\mathrm{W/(m^2\,sr)}$) and dE_j is the received irradiance.

The planetary surface BRDF directly leads to the albedo irradiance received by a target if the sun irradiance at the planet surface and the solid angle subtended by the target are known.

The target surface BRDF gives the direction in which the target is accelerated through integration over all directions $\mathbf{V}$ in which radiation is reflected. The unitless reaction vector, which includes both the direction and magnitude based on absorped, specularly and diffusely reflected fractions, is therefore [7]

$$\mathbf{R} = -\left[\mathbf{L} + \int_0^{2\pi}\int_0^{\pi/2} f_r \cos\theta_r \mathbf{V} d\theta_r d\phi_r\right]. \tag{2}$$

This vector encapsulates the mechanics of momentum transfer. The reaction is minimal for pure absorption ($f_r = 0$). The reaction is maximal (double the minimum) for pure specular reflection in the incidence direction.

Specular–diffuse reflectance distribution A simplified BRDF is usually more practical for RP modeling: the reflectance is assumed to be a mix of an ideal Lambertian diffuse component and a purely mirror-like specular components. Such a BRDF is given by [7]

$$f_r = C_d\frac{1}{\pi} + C_s\frac{\delta(\mathbf{V}-\mathbf{M})}{\cos\theta_i} \tag{3}$$

where C_d and C_s are the diffuse and specular reflectivity coefficients. Together with the absorption coefficient C_a, energy is conserved when $C_a + C_d + C_s = 1$. The vector $\mathbf{M} = 2\cos\theta_i\mathbf{N} - \mathbf{L}$ is the direction of $\mathbf{L}$'s mirror-like reflection, which only contributes if $\mathbf{V} = \mathbf{M}$.

For this simplified BRDF, the integral in Equation (2) evaluates analytically to [8]

$$\mathbf{R} = -\left[(C_a + C_d)\mathbf{L} + \frac{2}{3}C_d\mathbf{N} + 2\cos\theta_i C_s\mathbf{N}\right]. \tag{4}$$

If the target is in thermodynamic equilibrium, all absorbed radiation will be reradiated instantaneously by Kirchhoff's law. If this reradiation is Lambertian, the reaction vector becomes [8]

$$\mathbf{R} = -\left[(C_a + C_d)\left(\mathbf{L} + \frac{2}{3}\mathbf{N}\right) + 2\cos\theta_i C_s\mathbf{N}\right]. \tag{5}$$

The specular contribution is strictly along the surface normal direction since its tangential components cancel. The Lambertian diffuse contribution (both reflected and reradiated) has a component along the incoming direction but also, weighted by a factor $2/3$ (see [9] for a derivation of this factor), a component along the surface normal. The reaction vector will thus always be in the plane spanned by $\mathbf{L}$ and $\mathbf{N}$.

2.3 Radiation sources

Radiation sources emit or reflect radiation, which exerts RP onto the target. As explained in Section 2.1, the incident radiation at a target due to a source can be thought of as light rays, which are described by their directional irradiance at the target. How the directional irradiance is calculated depends on the type of source.

Isotropic point sources The simplest source model is a point source that isotropically radiates in all directions. This model is appropriate for far-away sources such as the Sun at $1\,\mathrm{au}$ distance. Due to the distance, all rays are effectively parallel and can be merged into a single ray parallel to the source–to–target vector $\mathbf{r}_{t/s}$. For an isotropic source, the total luminosity L (units of W) is uniformly distributed over a sphere, leading to an inverse square law. Therefore, the irradiance at the target is

$$E = \frac{L}{4\pi\left\|\mathbf{r}_{t/s}\right\|^2}. \tag{6}$$

Alternatively, a reference irradiance E_{ref} observed at a distance $\mathbf{r}_{\text{ref}}$ can be scaled:

$$E = E_{\text{ref}}\frac{r_{\text{ref}}}{\left\|\mathbf{r}_{t/s}\right\|^2}. \tag{7}$$

The solar luminosity is $3.828 \times 10^{26}\,\mathrm{W}$ [10], which corresponds to an irradiance of $1361\,\mathrm{W/m^2}$ at $1\,\mathrm{au}$. Note that these values are averages, which vary with the 11-year solar cycle by about $0.1\,\%$ and more on shorter timescales due to sunspot darkening and facular brightening [11]. Observational time series exist to account for these variations [12].

Paneled sources: Discretization Radiation due to planets and moons requires more involved source models. Planetary emissions comprise reflected solar radiation and thermal infrared radiation [13]. The fraction of reflected sunlight is called albedo a; the corresponding type is therefore also called albedo radiation. Thermal radiation is due to absorbed solar energy that is re-emitted in a delayed fashion. Observation time series of albedo and thermal fluxes exist for Earth [12], but physical modeling is required for the Moon.

Since planetary radiation is not isotropic and the spacecraft is typically much closer to the body than to the Sun, the source extent has to be considered. In contrast to the previously described point source, we therefore model Earth and Moon as extended sources. These are discretized into sub-sources, from which rays emanate that are, in general, not parallel. The sub-sources can be thought of as panels with an area, orientation, position, and radiosity model. The panel extent is represented by the area but any other panel properties are only evaluated at its center. A panel only radiates from the positive normal side, not from the backside.

Different algorithms exist to divide the planet ellipsoid into panels. Some authors use a longitude–latitude grid (e.g., [14, 15], particularly with observed fluxes) or generate static, uniformly spaced panels over the whole sphere (e.g., [7]). However, both approaches are inefficient for low-altitude spacecraft, which require a large number of panels, most of which are never visible. Therefore, the de-facto standard is the dynamic[1] paneling method introduced by Knocke *et al.* [13].

In Knocke's method, only the visible area of the planet is paneled. This area is a spherical cap, centered at the subsatellite point and divided into concentric rings that are, again, divided into equal-area segments. A central panel is located at the subsatellite point. All panels contribute to the irradiance received by the target. However, the effective area of each panel is projected by its viewing angle θ_r (see Figure 1) and the irradiance is attenuated by an inverse square law. In Knocke's method, the rings are spaced such that each panel has the same projected, attenuated area. The projected, attenuated area of a panel is defined as [13]

$$\frac{dA\cos\theta_r}{\left\|\mathbf{r}_{t/s}\right\|^2}, \tag{8}$$

where dA is the geometric panel area and $r_{t/s}$ is the source–to–target vector (in this case, the panel–to–target vector). More rings and more panels per ring will improve the fidelity of the calculated irradiance, barring the resolution limit of the radiosity model (e.g., the albedo distribution). While arbitrary numbers of panels per ring are possible, Knocke suggests multiples of 6 (i.e., six panels in the first ring, twelve panels in the second ring, ...). The algorithm is elaborated in [16].

Two examples at different spacecraft altitudes and with different ring numbers are shown in Figure 2. At higher altitudes, a larger area is visible (approaching a hemisphere) and panels are somewhat more uniform in area. At lower altitudes, the panels are more tightly spaced towards the subsatellite point. In both cases, panel areas increase towards the edge of the visible cap. This pattern is result of the equal projected, attenuated areas.

Paneled sources: Radiosity models The emitted and reflected fluxes of a panel are described by a radiosity model. The irradiance at the target position can then be derived from the panel radiosity. Both radiosity and irradiance commonly have units of $\mathrm{W/m^2}$. Each panel can have one or more radiosity model, usually one for albedo radiation and one for thermal radiation. We will now present three such models.

The albedo radiosity model accounts for diffuse Lambertian reflection of solar radiation. It implements the specular–diffuse BRDF from Equation (3) with $C_s = 0$ and the albedo value $C_d = a$ at the panel center. The albedo radiosity of a panel is [13]

$$J_{\text{albedo}} = a\left(\cos\theta_i\right)_+ E_s, \tag{9}$$

where E_s is the incoming solar irradiance at the panel (e.g., as found from Equation (6)) and the solar incidence angle θ_i is defined in Figure 1. The operator $(\cdot)_+$ restricts the input to positive values or zero otherwise. This ensures that no radiation is reflected from the backside.

The delayed thermal radiosity model assumes that absorbed radiation is emitted independently of incident solar radiation and the radiosity is thus not a function of θ_i. The only spatial variations arise from emissivity differences. The emissivity e of a surface is the ratio of the actual radiosity to the ideal black body radiosity. The delay arises from the planet's large thermal inertia. The delayed thermal radiosity of a panel is [13]

$$J_{\text{thermal}} = e\frac{E_s}{4}, \tag{10}$$

where e is the emissivity of the panel, evaluated at its center. The factor 1/4 is the ratio of absorbing area (a circle) to emitting area (a sphere).

The angle-based thermal radiosity model is more appropriate than the delayed model if the surface experience significant diurnal cooling and heating. The surface temperature is modeled as a function of the solar incidence angle θ_i and related to the radiosity through the Stefan–Boltzmann law. The surface temperature is interpolated between the minimum and maximum temperatures, T_{min} and T_{max} as

$$T = \max\left(T_{\text{max}}\left(\cos\theta_i\right)_+^{1/4}, T_{\text{min}}\right). \tag{11}$$

The angle-based thermal radiosity of a panel is then [17]

$$J_{\text{thermal}} = e\sigma T^4, \tag{12}$$

where T is the surface temperature from Equation (11) at the panel center and $\sigma = 5.670 \times 10^{-8}\,\mathrm{W/(m^2\,K^4)}$ is the Stefan–Boltzmann constant. The maximum radiosity of $e\sigma T_{\text{max}}^4$ is usually larger than the near-constant $eE_s/4$ from Equation (10), but quickly decreases as the panel moves away from the subsolar point (where $\theta_i = 0°$). On the nightside, the thermal radiosity reduces to $e\sigma T_{\text{min}}^4$.

To obtain the irradiance at the target due to the panel radiosity, we assume that the emission follows Lambert's

[1] Dynamic refers to the fact that panels move with the spacecraft, as opposed to static paneling, for which panels are invariant with spacecraft position or time.

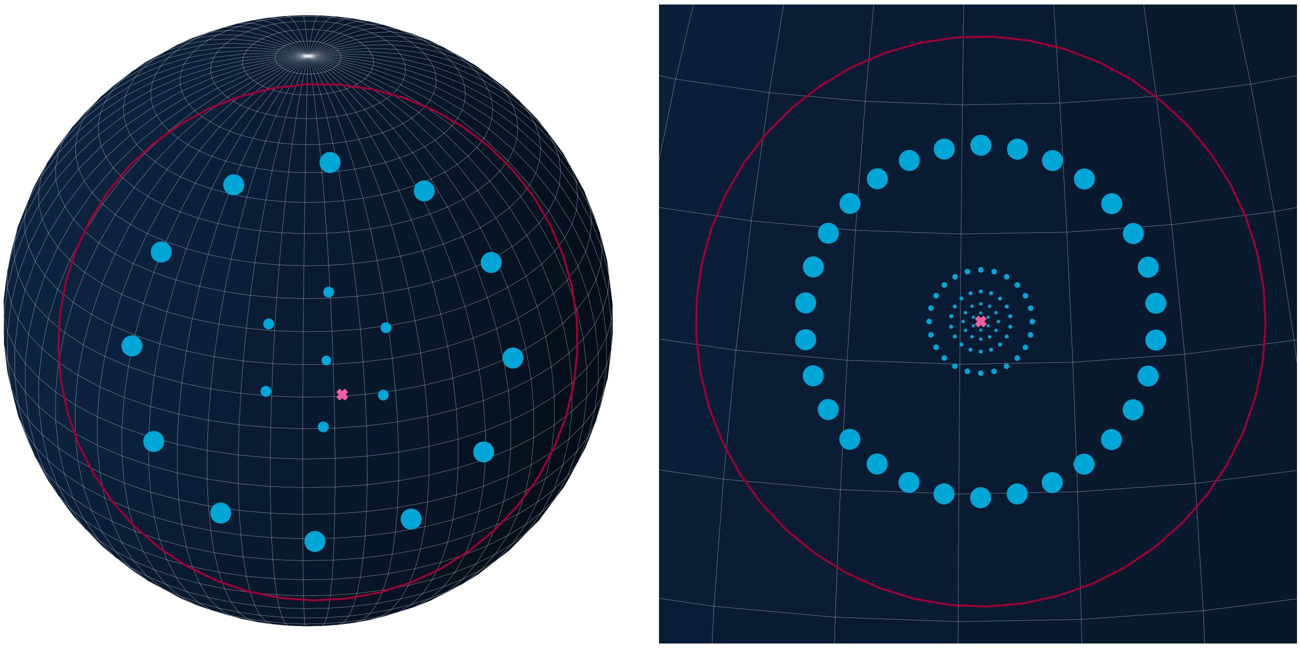

(a) High altitude: $h = 1500$ km, 2 rings, angular diameter of cap = 115°. **(b)** Low altitude: $h = 50$ km, 5 rings, angular diameter of cap = 27°.

Figure 2. Panels generated with Knocke's algorithm for the Moon, which has a polar radius of 1737 km. The spacecraft (✖) sees a spherical cap (—), which contains rings of panels and is larger at higher altitudes h. Panel centers (●) are scaled proportional to the panel area. The panels have equal projected, attenuated areas and are therefore concentrated around the subsatellite point.

cosine law and account for the projected, attenuated area of the source panel. The irradiance therefore is

$$E = \left(\sum_{J_i \in \mathcal{J}} J_i \right) \frac{dA \left(\cos \theta_r \right)_+}{\pi \left\| \mathbf{r}_{t/s} \right\|^2}, \tag{13}$$

where $\mathcal{J}$ is the set of radiosities from any of the previous radiosity models. Usually, a panel has the albedo model and one thermal model. Here, the source–to–target vector $\mathbf{r}_{t/s}$ uses the panel center position, not the source body center. The direction $\hat{\mathbf{r}}_{t/s}$ of the corresponding directional irradiance $\mathbf{E} = E\hat{\mathbf{r}}_{t/s}$ is therefore not the same for each panel and thus accounts for the extent of the source. The radiosities J_i in Equation (13) can be summed since their radiation emanates from the same point, the panel center. Contrarily, the directional irradiances $\mathbf{E}$ can generally not be summed since the their individual directions need to be retained: the reflectance model of the target may be sensitive to the incoming direction of each ray. Therefore, a set of directional radiances $\mathcal{E}$ is handed to the RP target model for acceleration calculations.

2.4 Radiation pressure targets

A RP target is a body that is accelerated by RP. The target model governs how the incident irradiances from point sources and extended sources accelerate the target body.

Cannonball target In its simplest form, a target can be modeled as isotropic sphere, also referred to as cannonball. This sphere is characterized by a cross-sectional area A_c (independent of orientation), radiation pressure coefficient C_r (incorporating reflectivity and absorption coefficients), and mass m. Due to its isotropy, any lateral components cancel and the net acceleration is always along the source–to–target vector. The RP acceleration of a cannonball target is [18]

$$\mathbf{a} = C_r \frac{A_c}{m} \sum_{\mathbf{E}_j \in \mathcal{E}} \frac{\mathbf{E}_j}{c}, \tag{14}$$

where the sum is vectorial and $\sum \mathbf{E}_j / c$ is the total RP as described in Section 2.1. $\mathcal{E}$ is the set of directional irradiances from any number of sources, both point (Equation (6)) and paneled (Equation (13)). The dependence on the area-to-mass ratio A_c/m is similar to drag accelerations. While the cannonball model cannot account for complex geometry, it is often used in orbit determination with C_r as estimated variable.

Paneled target In reality, the cross-section and optical properties of a spacecraft change with orientation and incident direction. This effect is particularly noticeable for solar panels, which are large and usually track the Sun. To account for the geometry and differences in materials, a spacecraft can be represented as a collection of n panels. Each panel is characterized by its area, surface normal, and reflectance distribution. In case of moving parts, the surface normal may change over time. The reflectance distribution can be given as generic BRDF, but is often a specular–diffuse BRDF. The RP acceleration of a paneled target is [19]

$$\mathbf{a} = \frac{1}{m} \sum_{\mathbf{E}_j \in \mathcal{E}} \left(\frac{\left\| \mathbf{E}_j \right\|}{c} \sum_{k=1}^{n} A_k \left(\cos \theta_{i,k} \right)_+ \mathbf{R}_k \right), \tag{15}$$

where the indices j and k denote the (sub-)source and target panel, respectively. A_k is the area of the k-th panel. $\theta_{i,k}$ is the incidence angle of $\mathbf{E}_i$ onto the k-th panel. $\mathbf{R}_k$ is the reaction vector as defined by Equations (2), (4) or (5), depending on the BRDF. The reaction vector is a function of the panel surface normal $\mathbf{N}$ and the source–to–target direction

$\mathbf{L} = \hat{\mathbf{E}}_j$. Therefore, the inner sum has to be evaluated for each directional irradiance $\mathbf{E}_j$ of the outer sum. In general, the resulting acceleration will not be along the source–to–target direction as for the cannonball.

Extensions for the paneled target model exist. The model described above does not account for self-shadowing, which is occurs when one ray would intersect two panels. This effectively reduces the area of the shadowed panel, an effect that can be significant for complex spacecraft geometries [20]. Polygon intersections enable simple calculation of the effective area [20]. Ray tracing is more involved but can also account for multiple reflections between target panels [21].

Another extension is the radiation pressure due to thermal radiation of the spacecraft itself. Instantaneous reradiation as modeled by Equation (5) for the case of thermodynamic equilibrium is a simple version of this. In reality, panels heat up and cool down (particularly during eclipses) through radiation, conduction, and internal heat production. Advanced models therefore calculate the temperature of each panel. Such models range from a simple heat balance [7] to finite element models [15]. However, lack of knowledge of the thermal properties may restrict the applicability. For the sake of simplicity, neither self-shadowing nor thermal radiation pressure of the spacecraft will be considered in this paper.

2.5 Occultation

All previous models that the line of sight between source and target is unobstructed. However, eclipses are a common astronomical phenomenon: a low altitude spacecraft may be in the planet's shadow for more than a third of its period, and partial or full lunar eclipses can occur multiple times per year. We present two occultation models.

Shadow function The shadow function ν describes the fraction of light received from a spherical source in the presence of an occulting spherical body. The geometry of the conical occultation model is shown in Figure 3. In the umbra, the source is fully occulted and the observer does not receive any radiation ($\nu = 0$), a state referred to as total eclipse. In the penumbra, the observer can see part of the source ($0 < \nu < 1$). Only outside the shadow region does the observer receive the full radiation ($\nu = 1$). In the case of a lunar eclipse, Earth occults the Sun and casts a shadow onto the Moon such that there is no lunar albedo radiation. On the nightside of a planet, the planet itself occults the Sun.

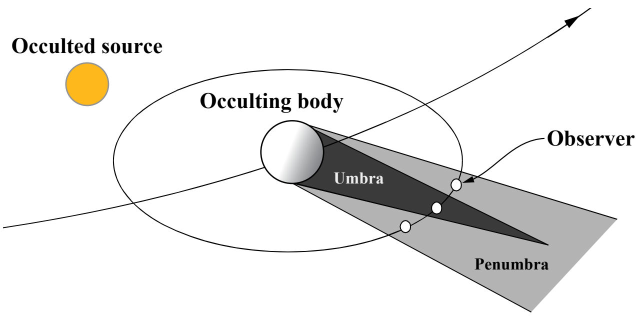

Figure 3. Conical occultation model for spherical sources and occulting bodies. The observer is partially illuminated in the penumbra but fully shadowed in the umbra. Adapted from [22].

In the framework of models previously defined, the shadow function needs to be considered both for direct radiation from a point source and for the solar radiation used for albedo radiosity. The extent of the source and occulting bodies needs to be known for shadow function calculations, even in the case of point sources. A derivation of conical model for ν is presented by Montenbruck and Gill [18].

The conical model can only account for one occulting body. In case of multiple occulting bodies, shadows might overlap and the product of their shadow functions would underestimate the actual received fraction. Knowledge of the shadow intersection would be required to avoid this. Zhang *et al.* derived a model for two occulting bodies [23]. However, only single occultations will be considered in this paper.

More involved shadow models exist that improve prediction of the penumbra passage. These models can account for planetary oblateness and atmospheric effects like absorption, scattering and refraction [24]. Other models can account for topography by combining a paneled Sun model with topography map [25]. These modification usually prolong the penumbra duration.

Point-to-point visibility For source panels represented by their center, the shadow function becomes binary: either there is a line of sight between the panel center and the target or there is not. Such point-to-point visibility with a spherical occulting body is easily modeled geometrically. A derivation is given by Vallado and Wertz [22]. Multiple occultations are supported by this occultation model by the logical conjunction of the individual visibilities.

3 Radiation pressure modeling for LRO

3.1 Lunar radiation pressure

use 5 rings for moon due to convergence analysis and results from [4] [26] also uses 5 rings for LRO Need more with DLAM-1 than knocke due to higher frequency albedo dist or lower altitude?

no seasonal or diurnal albedo variation on Moon, as opposed to Earth [16]

Knocke argues that Earth can be reasonably represented using diffuse albedo reflection only this is not the case for moon, particularly at low phase angles [27] However, this is only relevant for small beta angles, and even then only small fractions of orbit (would increase radial magnitude over subsolar point?) therefore, beyond scope of the paper

actual hapke parameter map in [28]

albedo value used should be for broadband shortwave ($0.2\,\mu m$ to $4\,\mu m$, peak at $0.4\,\mu m$) [16], which accounts for most of solar radiation albedo used for moon is 0.19 (750 nm, which corresponds to maximum reflectivity [4]), which is mean of DLAM-1, even though 0.12 is commonly cited DLAM-1 is derived from clementine imagery, which is known to overestimate albedo [27] This is to enable better comparison, but if a constant albedo value were used, this amounts to linear scaling

use angle-based model from Lemoine Flux from Lemoine agrees with [29, Table 8]

Constant-emission model from Knocke is not appropriate for moon since it gets very cold -¿ Knocke would result in constant emission (only varies by XX% due to change in Moon–Sun distance), will not be investigated further here

3.2 LRO target

to find cannonball area and coefficient, some authors use raytracing [30], we just use weighted average finding a single rp coefficien is virtually impossible since it changes [22, p 580]

Different values for A and Cr in literature: [26]: 14, 1.0 (for daily/not precision OD, no changing orientation, solar only) –¿ use this one [31]: 10, 1.2 (no changing orientation, solar only) [3]: first 1.67, then 0.96 after estimation [25]: 1.03 +- 0.24 (1.04 in sep, 1.4 in jun, but rather a scale factor for paneling than cannonball coefficient)

mass at start of science orbit (15 Sep 2009): 1271.9 kg mass at end of science orbit (11 Dec 2011): 1087.0 kg use end of science orbit mass for all scenarios to get worst case scenario fixed mass to enable comparison also show mass history

effect of self-shadowing on LRO orbit is small [32] neglecting self-shadowing overestimates area [20], but minimal self-shadowing in most cases for LRO [3]

instantaneous reradiation will not be investigated further describe how results change (simple scaling?) Thermal radiation may cause an offset of 1-2 meters over an arclength of 2.5 days [31]

3.3 LRO orbit geometry

variation in altitude is in part due to assumption of spherical moon (polar radius is 2.1 km less than equatorial) -¿ leads to change in lunar RP magnitude over orbit sun beta over year + eclipse periods

our maximum eclipse time of 48 min agrees with [29]

describe beta angle maybe figure with orbit geometry for simulated arcs

3.4 Simulation setup

simulation setup in table, explanations in text

earth albedo + thermal radiation can be neglected for LRO since it is less than 0.1% of solar radiation at moon

solar array tracks Sun, HGA tracks Earth [29] start at start at 26 June 2010 06:00:00 Earth eclipses Sun during this time Moon does not eclipse Sun (Sun beta angle is about -90 deg, see [29])

lunar eclipses avoided since we cannot represent multiple occultations

effects of neglecting terrain and self shadowing [25] sec 4.2 and 4.3

Operational LRO OD does not use lunar albedo due to computational demand, but used for offline reprocessing. Self-shadowing from Mazarico *et al.* is used for reprocessing [26]

arc length 2.5 days, which is also used for LRO orbit determination [33] step 5 s, which is also used for LRO orbit determination [25]

MOON_PA frame, IAU_MOON is in worst case 155 m off [34] (Special PCK and FK for Earth and Moon, slide 14)

integrator + propagator params

two arcs, one for beta = 0 and beta = 90 describe why These

4 Results

no knowledge of true RP accelerations therefore, compare to baseline

Also use [35] as reference for plots and discussion, especially about relation of acc and change in elements

4.1 Simulation setups

Solar with/without Lunar with/without Albedo constant/dlam LRO cannonball/paneled Occultation with/without (for solar only?)

4.2 Accelerations

thermal vs albedo

kink in cross-track SRP also seen in SELENE [36], search for explanation

Variation with orbital position and time of year (correlate with relative sun position and albedo map)

beta angle slightly less than 90 degrees leads to sinusoidal acceleration

show partial/full eclipse on time axis

absolute acceleration magnitude influenced by mass uncertainty rp acceleration magnitude increases as mass decreases 17% higher mass at start -¿ 17 % lower acceleration magnitude

angle-based thermal behaves quite similar to albedo, but does not vanish in eclipse

4.3 Change in orbital element

compare wih Gauss perturbing equations (analytical solution to change of osculating elements based on accelerations), e.g. [37, Sec. 3.2]

4.4 Performance

no special setup like cpu pinning or disabled hyperthreading for benchmarking only on one setup Performance may vary in other situations [38] still, a good indication also mention minimum

albedo model can increase computational demand by several hundred pct [26]

5 Discussion & Conclusion

"It would seem, therefore, that the influence of the longwave emitted radiation would be almost indistinguishable from a small change in the gravitational constant of the Earth, for low eccentricity orbits. As a consequence, one would expect the shortwave component to have a greater orbital effect than the longwave component, in spite of the comparable magnitudes of their accelerations." [16]

recommendations on which models to use

Future work:

- account for moon topography for occlusion [25], could otherwise lead to large misrepresentation of eclipses for $\beta > 70°$
- Self-shadowing, particularly for SRP, can reduce effective cross section by up to 40 % [25]
- accurate thermal reradiation (e.g. [39])

- account for non-diffuse reflection of lunar surface, i.e.opposition effect due to shadow hiding and coherent backscatter, which can greatly increase irradiance at small phase angles [40] (this would only be relevant at beta = 0 since low phase angles do not occur for large betas; phase angle is low if target is above subsolar point); a map of Hapke parameters exists [**Sako2014**]

References

1. M. T. Zuber *et al.*, "The Lunar Reconnaissance Orbiter Laser Ranging Investigation," *Space Science Reviews*, vol. 150, no. 1-4, pp. 63–80, May 2009. DOI: 10.1007/s11214-009-9511-z.
2. G. Chin *et al.*, "Lunar Reconnaissance Orbiter Overview: The Instrument Suite and Mission," *Space Science Reviews*, vol. 129, no. 4, pp. 391–419, May 2007. DOI: 10.1007/s11214-007-9153-y.
3. S. Slojkowski, J. Lowe, and J. Woodburn, "Orbit determination for the lunar reconnaissance orbiter using an extended Kalman filter," in *International Symposium on Space Flight Dynamics (ISSFD) 2015*, 2015.
4. R. Floberghagen, P. Visser, and F. Weischede, "Lunar albedo force modeling and its effect on low lunar orbit and gravity field determination," *Advances in Space Research*, vol. 23, no. 4, pp. 733–738, Jan. 1999. DOI: 10.1016/s0273-1177(99)00155-6.
5. S. E. Slojkowski, "Lunar Reconnaissance Orbiter orbit determination accuracy analysis," in *International Symposium on Space Flight Dynamics*, 2014.
6. G. Kopp and J. L. Lean, "A new, lower value of total solar irradiance: Evidence and climate significance," *Geophysical Research Letters*, vol. 38, no. 1, n/a–n/a, Jan. 2011. DOI: 10.1029/2010gl045777.
7. C. J. Wetterer *et al.*, "Refining Space Object Radiation Pressure Modeling with Bidirectional Reflectance Distribution Functions," *Journal of Guidance, Control, and Dynamics*, vol. 37, no. 1, pp. 185–196, Jan. 2014. DOI: 10.2514/1.60577.
8. O. Montenbruck, P. Steigenberger, and U. Hugentobler, "Enhanced solar radiation pressure modeling for Galileo satellites," *Journal of Geodesy*, vol. 89, no. 3, pp. 283–297, Nov. 2014. DOI: 10.1007/s00190-014-0774-0.
9. M. Ziebart, "Generalized Analytical Solar Radiation Pressure Modeling Algorithm for Spacecraft of Complex Shape," *Journal of Spacecraft and Rockets*, vol. 41, no. 5, pp. 840–848, Sep. 2004. DOI: 10.2514/1.13097.
10. A. Prša *et al.*, "NOMINAL VALUES FOR SELECTED SOLAR AND PLANETARY QUANTITIES: IAU 2015 RESOLUTION B3," *The Astronomical Journal*, vol. 152, no. 2, p. 41, Aug. 2016. DOI: 10.3847/0004-6256/152/2/41.
11. G. Kopp, "Magnitudes and timescales of total solar irradiance variability," *Journal of Space Weather and Space Climate*, vol. 6, A30, 2016. DOI: 10.1051/swsc/2016025.
12. S. Dewitte and N. Clerbaux, "Measurement of the Earth Radiation Budget at the Top of the Atmosphere—A Review," *Remote Sensing*, vol. 9, no. 11, p. 1143, Nov. 2017. DOI: 10.3390/rs9111143.
13. P. Knocke, J. Ries, and B. Tapley, "Earth radiation pressure effects on satellites," in *Astrodynamics Conference*, American Institute of Aeronautics and Astronautics, Aug. 1988. DOI: 10.2514/6.1988-4292.
14. C. J. Rodriguez-Solano, U. Hugentobler, P. Steigenberger, and S. Lutz, "Impact of Earth radiation pressure on GPS position estimates," *Journal of Geodesy*, vol. 86, no. 5, pp. 309–317, Oct. 2011. DOI: 10.1007/s00190-011-0517-4.
15. F. Wöske, T. Kato, B. Rievers, and M. List, "GRACE accelerometer calibration by high precision non-gravitational force modeling," *Advances in Space Research*, vol. 63, no. 3, pp. 1318–1335, Feb. 2019. DOI: 10.1016/j.asr.2018.10.025.
16. P. Knocke, "Earth radiation pressure effects on satellites," Ph.D. dissertation, The University of Texas at Austin, 1989.
17. F. G. Lemoine *et al.*, "High–degree gravity models from GRAIL primary mission data," *Journal of Geophysical Research: Planets*, vol. 118, no. 8, pp. 1676–1698, Aug. 2013. DOI: 10.1002/jgre.20118.
18. O. Montenbruck and E. Gill, *Satellite Orbits*. Springer Berlin Heidelberg, Dec. 2000, 371 pp. DOI: 10.1007/978-3-642-58351-3.
19. J. Marshall, S. Luthcke, P. Antreasian, and G. Rosborough, "Modeling radiation forces acting on TOPEX/Poseidon for precision orbit determination," Goddard Space Flight Center, Tech. Rep. NASA-TM-104564, 1992.
20. E. Mazarico, M. T. Zuber, F. G. Lemoine, and D. E. Smith, "Effects of Self-Shadowing on Nonconservative Force Modeling for Mars-Orbiting Spacecraft," *Journal of Spacecraft and Rockets*, vol. 46, no. 3, pp. 662–669, May 2009. DOI: 10.2514/1.41679.
21. P. W. Kenneally and H. Schaub, "Fast spacecraft solar radiation pressure modeling by ray tracing on graphics processing unit," *Advances in Space Research*, vol. 65, no. 8, pp. 1951–1964, Apr. 2020. DOI: 10.1016/j.asr.2019.12.028.
22. D. A. Vallado and J. Wertz, *Fundamentals of Astrodynamics and Applications, 4^{th} ed.* Microcosm Press, 2013, p. 1106.
23. R. Zhang, R. Tu, P. Zhang, J. Liu, and X. Lu, "Study of satellite shadow function model considering the overlapping parts of Earth shadow and Moon shadow and its application to GPS satellite orbit determination," *Advances in Space Research*, vol. 63, no. 9, pp. 2912–2929, May 2019. DOI: 10.1016/j.asr.2018.02.002.
24. Z. Li, M. Ziebart, S. Bhattarai, and D. Harrison, "A shadow function model based on perspective projection and atmospheric effect for satellites in eclipse," *Advances in Space Research*, vol. 63, no. 3, pp. 1347–1359, Feb. 2019. DOI: 10.1016/j.asr.2018.10.027.

25. E. Mazarico, G. A. Neumann, M. K. Barker, S. Goossens, D. E. Smith, and M. T. Zuber, "Orbit determination of the Lunar Reconnaissance Orbiter: Status after seven years," *Planetary and Space Science*, vol. 162, pp. 2–19, Nov. 2018. DOI: 10.1016/j.pss.2017.10.004.

26. A. Nicholson, S. Slojkowski, A. Long, M. Beckman, and R. Lamb, "NASA GSFC Lunar Reconnaissance Orbiter (LRO) Orbit Estimation and Prediction," in *SpaceOps 2010 Conference*, American Institute of Aeronautics and Astronautics, Apr. 2010. DOI: 10.2514/6.2010-2328.

27. Y. Shkuratov, V. Kaydash, V. Korokhin, Y. Velikodsky, N. Opanasenko, and G. Videen, "Optical measurements of the Moon as a tool to study its surface," *Planetary and Space Science*, vol. 59, no. 13, pp. 1326–1371, Oct. 2011. DOI: 10.1016/j.pss.2011.06.011.

28. H. Sato, M. S. Robinson, B. Hapke, B. W. Denevi, and A. K. Boyd, "Resolved Hapke parameter maps of the Moon," *Journal of Geophysical Research: Planets*, vol. 119, no. 8, pp. 1775–1805, Aug. 2014. DOI: 10.1002/2013je004580.

29. C. R. Tooley *et al.*, "Lunar Reconnaissance Orbiter Mission and Spacecraft Design," *Space Science Reviews*, vol. 150, no. 1-4, pp. 23–62, Jan. 2010. DOI: 10.1007/s11214-009-9624-4.

30. A. Hattori and T. Otsubo, "Time-varying solar radiation pressure on Ajisai in comparison with LAGEOS satellites," *Advances in Space Research*, vol. 63, no. 1, pp. 63–72, Jan. 2019. DOI: 10.1016/j.asr.2018.08.010.

31. S. Bauer *et al.*, "Demonstration of orbit determination for the Lunar Reconnaissance Orbiter using one-way laser ranging data," *Planetary and Space Science*, vol. 129, pp. 32–46, Sep. 2016. DOI: 10.1016/j.pss.2016.06.005.

32. A. Löcher and J. Kusche, "Precise orbits of the Lunar Reconnaissance Orbiter from radiometric tracking data," *Journal of Geodesy*, vol. 92, no. 9, pp. 989–1001, Feb. 2018. DOI: 10.1007/s00190-018-1124-4.

33. E. Mazarico *et al.*, "Orbit determination of the Lunar Reconnaissance Orbiter," 3, vol. 86, Springer Science and Business Media LLC, Sep. 2011, pp. 193–207. DOI: 10.1007/s00190-011-0509-4.

34. Navigation and Ancillary Information Facility, *SPICE Tutorials*, Jan. 2020.

35. N. Borderies and P.-y. Longaretti, "A new treatment of the albedo radiation pressure in the case of a uniform albedo and of a spherical satellite," *CELESTIAL MECHANICS AND DYNAMICAL ASTRONOMY*, vol. 49, no. 1, pp. 69–98, 1990. DOI: 10.1007/bf00048582.

36. T. Kubo-oka and A. Sengoku, "Solar radiation pressure model for the relay satellite of SELENE," *Earth, Planets and Space*, vol. 51, no. 9, pp. 979–986, Sep. 1999. DOI: 10.1186/bf03351568.

37. D. M. Lucchesi and V. Iafolla, "The Non-Gravitational Perturbations impact on the BepiColombo Radio Science Experiment and the key rôle of the ISA accelerometer: direct solar radiation and albedo effects," *Celestial Mechanics and Dynamical Astronomy*, vol. 96, no. 2, pp. 99–127, Oct. 2006. DOI: 10.1007/s10569-006-9034-9.

38. T. Mytkowicz, A. Diwan, M. Hauswirth, and P. F. Sweeney, "Producing wrong data without doing anything obviously wrong!" *ACM SIGPLAN Notices*, vol. 44, no. 3, pp. 265–276, Feb. 2009. DOI: 10.1145/1508284.1508275.

39. J. A. Marshall and S. B. Luthcke, "Modeling radiation forces acting on Topex/Poseidon for precision orbit determination," *Journal of Spacecraft and Rockets*, vol. 31, no. 1, pp. 99–105, Jan. 1994. DOI: 10.2514/3.26408.

40. B. J. Buratti, J. K. Hillier, and M. Wang, "The Lunar Opposition Surge: Observations by Clementine," *Icarus*, vol. 124, no. 2, pp. 490–499, Dec. 1996. DOI: 10.1006/icar.1996.0225.